The forecast of predictability for computed orbits in galactic models

J. C. Vallejo[1,2]★ and M. A. F. Sanjuán[2]

[1]*European Space Astronomy Centre, PO Box 78, E-28691 Villanueva de la Canada, Madrid, Spain*
[2]*Nonlinear Dynamics, Chaos and Complex Systems Group, Departamento de Física, Universidad Rey Juan Carlos, Tulipan s/n, E-28933 Mostoles, Madrid, Spain*

ABSTRACT

The predictability of a system indicates how much time a computed orbit is close to an actual orbit of the system, independent of its stability or chaotic nature. We derive a predictability index from the distributions of finite-time Lyapunov exponents of several prototypical orbits, both regular and irregular, in a variety of galactic potentials. In addition, by analysing the evolution of the shapes of the distributions with the finite-time intervals sizes, we get an insight into the time-scales of the model when the flow dynamics evolve from the local to the global regime.

Key words: methods: numerical – galaxies: haloes – galaxies: kinematics and dynamics.

1 INTRODUCTION

With the widespread use of computer simulations to solve complex dynamical systems, the reliability of numerical calculations is of increasing interest. This reliability is directly related to the regularity and instability properties of the analysed orbits. In this scenario, the modelling of galactic potentials is an interdisciplinary field, where the astrophysics field provides the simulated models, the non-linear dynamics field provides the chaoticity and instability properties and the computational sciences provide the actual numerical implementation.

The gravitational *N*-body simulation is a common tool to study the evolution of the galaxies and the formation of their features. The galaxy is modelled as a self-gravitating system containing stars, gas particles and dark matter, all of them modelled as point-like masses. The self-consistency of these models captures very well the necessary details of the galactic dynamics, however, the available computational resources impose a limit to the number of particles to be taken into account. This usually implies an artificial smoothing of the potential and a proper handling of the required scaling parameters.

As an alternative, another approach that might be taken, is the use of simulations based in a single mean field potential. As there are no collisions among particles, the dynamics of a galaxy can be considered to be formed by independent trajectories within the global potential where the motion of each star is just driven by a continuous smooth potential. A dynamical model usually mathematically describes the potential as a function of the distance from the centre of the galaxy. Some potentials are derived at specific snapshots of the *N*-body simulations and some others are selected to physically represent desired characteristics of the galaxies.

Although these simulations are driven by fully deterministic equations, some of these systems exhibit a strong sensitivity on the initial conditions, which manifests itself in the form of chaotic behaviour. Many works have characterized the presence of chaos through the computation of the standard asymptotic Lyapunov exponents. These are indicators on the globally averaged chaoticity of the system during an infinite integration time, but due to the sometimes slow convergence towards the asymptotic value, many other numerical indexes and fast averaged indicators have been developed aiming to distinguish between regular and chaotic orbits. We can cite, among others, the rotation index (Voglis, Contopoulos & Efthymiopoulos [1999]), the smaller alignment index (Skokos [2001]), its generalization, the generalized alignment *k*-index (Skokos, Bountis & Antonopoulos [2007]), the mean exponential growth factor of nearby orbits (Cincotta & Simó [2000]), the fast Lyapunov indicator (Froeschlé & Lega [2000]), the relative Lyapunov indicator (Sandor et al. [2004]) or the finite-time rotation number (Szezech et al. [2013]).

As a general result, regular orbits, such as box and tube orbits, are responsible for a major part of the shape of the galaxy, forming the skeleton of the observed mass density distributions, but still a high fraction of the orbits are chaotic. These chaotic orbits populate areas that are not accessible to the regular orbits, and may explain some observed structures like bars and bulges. They can also produce flows of matter which may locally enhance the star formation rate: see e.g. Olle & Pfenigger ([1998]), Pichardo, Martos & Moreno ([2004]), Contopoulos & Harsoula ([2013]) and Carpintero, Muzzio & Navone ([2014]).

Regarding the role of the dark haloes, the variety of these haloes shapes indicates their structure plays an important role in the dynamics of the galaxies. One of the predictions of the cold dark matter models is that galaxy-scale dark matter haloes are described by triaxial density ellipsoids. Dark triaxial haloes introduce a non-linear coupling that increases the degree of chaoticity and may affect the

★ E-mail: juan.carlos.vallejo@esa.int

goodness of the computed orbits. Depending on the degree of triaxiality, the phase space of a logarithmic potential can be occupied to a large extent by chaotic orbits (Papaphilippou & Laskar 1998; Caranicolas & Zotos 2010; Zotos & Caranicolas 2013; Zotos 2014).

Our work aims to analyse the predictability of the underlying models used to run the simulations. The predictability of a system indicates how long a computed orbit is close to an actual orbit, and this concept is related to, but independent of, its stability or its chaotic nature. A system is said to be chaotic when it exhibits strong sensitivity to the initial conditions. This means that the exact solution and a numerical solution starting very close to it may diverge exponentially one from each other. The predictability aims to characterize if this numerically computed orbit may be sometimes sufficiently close to another true solution, so it may be still reflecting real properties of the model, leading to correct predictions. The real orbit is called a shadow, and the noisy solution can be considered an experimental observation of one exact trajectory. The distance to the shadow is then an observational error, and within this error, the observed dynamics can be considered reliable (Sauer, Grebogi & Yorke 1997).

The shadowing property characterizes the validity of long computer simulations, and how they may be *globally* sensitive to small errors. The shadows can exist, but it may happen that, after a while, they may go far away from the true orbit. Consequently, a proper estimation of the shadowing times is a key issue in any simulation and provides an indication about its predictability. This shadowing time is directly linked to the hyperbolic or non-hyperbolic nature of the orbits. Hyperbolic systems are *structurally* stable in the sense that the shadowing is present during long times and numerical trajectories stay close to the true ones. In the case of non-hyperbolicity, an orbit may be shadowed, but only for a very short time, and the computed orbit behaviour may be completely different from the true orbit after this period.

The calculation of the shadowing times was already applied to the field of *N*-body simulations in Hayes (2003), where an iterative refinement method was applied to simulate noisy trajectories and to estimate the shadowing times. Less attention has been paid to the shadowing computation in the field of simulations of self-consistent models based in a single mean potential. The main goal of this work is to study the predictability of orbits of massless particles in galactic-type Hamiltonian systems. This predictability is computed through the use of finite-time Lyapunov exponents distributions following similar techniques to those described in Vallejo & Sanjuán (2013).

Our motivation, when selecting finite-time Lyapunov exponents techniques, is that they can be used in systems where asymptotic global results are of no interest, are not physically meaningful or may not even exist. We could also be interested in the analysis of transients periods, which just exist for a while before the system reaches a final stationary state. Or it may happen that because of the physics of the system, the time-scales for obtaining the global properties are too long to be realistic, since the galactic potential (or even the whole Universe) may have evolved for such a period.

The structure of the paper is the following. Section 2 reviews how the finite-time Lyapunov exponents distributions are built and how the predictability can be computed from them. Section 3 presents the selected numerical methods for calculating these distributions in conservative systems. Section 4 applies these techniques to representative orbits in simple meridional potentials. Section 5 applies these techniques to a more realistic Milky Way-type potential, including a triaxial dark halo. Finally, Section 6 summarizes the results and makes some concluding remarks.

2 PREDICTABILITY THROUGH FINITE-TIME LYAPUNOV EXPONENTS

This section presents how the predictability of the system can be derived from the computation of finite-time Lyapunov exponents distributions, as these distributions reflect the hyperbolic or non-hyperbolic nature of the dynamics.

2.1 Finite-time Lyapunov exponents distributions

The ordinary, or *asymptotic* Lyapunov exponent, describes the evolution in time of the distance between two nearly initial conditions, by averaging the exponential rate of divergence of the trajectories. It can be defined as

$$\lambda(\boldsymbol{x}, \boldsymbol{v}) = \lim_{t \to \infty} \frac{1}{t} \ln \| D\boldsymbol{\phi}(\boldsymbol{x}, t)\boldsymbol{v} \|, \tag{1}$$

provided this limit exists (Ott & Yorke 2008). Here, $\boldsymbol{\phi}(\boldsymbol{x}, t)$ denotes the solution of the flow equation, such that $\boldsymbol{\phi}(\boldsymbol{x}_0, 0) = \boldsymbol{x}_0$, and D is the spatial derivative in the direction of an infinitesimal displacement $\boldsymbol{v}$.

The *finite-time* Lyapunov exponents definition is derived from the standard asymptotic Lyapunov exponent for finite averaging times, as follows:

$$\chi(\boldsymbol{x}, \boldsymbol{v}, t) = \frac{1}{t} \ln \| D\boldsymbol{\phi}(\boldsymbol{x}, t)\boldsymbol{v} \|, \tag{2}$$

with the implicit dependence on the point $\boldsymbol{x}$ and the deviation vector $\boldsymbol{v}$. These finite-time Lyapunov exponents are sometimes named *effective* Lyapunov exponents when the intervals used to compute them are large enough, and the distributions can be analysed from the cumulant generating function (Grassberger, Badii & Politi 1988).

If we make a partition of the whole integration time along one orbit into a series of time intervals of size Δt, then it is possible to compute the finite-time Lyapunov exponent $\chi(\Delta t)$ for every interval and to plot its distribution. Obviously, $\lambda = \chi(\Delta t \to \infty)$. These distributions depend on the choice of the finite interval length, the initial directions of perturbation vectors and the total integration time used to compute the distribution.

By plotting the distribution of values obtained starting from a given initial condition, we can study the presence of the shadowing property. Our method relies in the fact of making a partition of the whole integration time along one selected initial condition into a series of time intervals of size Δt, instead of building the distribution from an ensemble of initial conditions belonging to the same dynamical domain (Vallejo, Aguirre & Sanjuan 2003).

2.2 Shadowing

The shadowing time τ measures how long a numerical trajectory remains valid by staying close to a true orbit. The shadowing distance is the local phase-space distance between both of them. This distance can be described as a diffusion equation of a particle, which may find different escape routes along its trajectory. The larger shadowing times become improbable due to the diffusion processes. The model described in Sauer (2002) assumes an exponential distribution of log shadowing distances to follow a biased random walk with drift towards a reflecting barrier. The expected shadowing time have power-law dependencies on the size of the one-step error made in a computer simulation, linked to the computer precision δ.

A sign of bad shadowing is the fluctuating behaviour around zero of the closest to zero finite-time Lyapunov exponent. Plotting

the finite-time distribution and assuming both the mean m and the standard deviation σ to be very small, the shadowing time τ is given by

$$\tau \sim \delta^{-h}, \qquad h = \frac{2\|m\|}{\sigma^2}. \qquad (3)$$

The exponent h is the hyperbolicity index, or predictability index. We will use it as an indicator of the predictability of the orbits. The lowest predictability occurs when h is very small and there is no improvement in τ, even for large values of δ. Conversely, the larger the h index, the better the shadowing.

This scaling law is closely related to intermittency, and can be considered 'intermittency in miniature'. The exponential distribution is the result of small excursions that periodically move the computed trajectory away from the true trajectory, and then return towards it. The assumption is that the motion follows a biased random walk, with a drift towards a reflecting barrier. The flow sometimes goes in one direction, far away from the true solution, and sometimes moves towards it. The reflecting barrier is caused by the single-step error δ, since new errors are created at each step, so the computed trajectory can never be expected to be closer than δ to the true trajectory.

A dynamical system is hyperbolic if the phase space can be spanned locally by a fixed number of independent stable and unstable directions, which are consistent under the operation of the dynamics and the angle between the stable and unstable manifolds is away from zero (Viana & Grebogi 2000; Kantz et al. 2002). In hyperbolic regions, the shadowing theory guarantees the existence of a nearby true trajectory. The exponents oscillate around zero because the shadowing distance swaps from exponential increases to exponential decreases, mimicking a random walk. In a non-hyperbolic region, a normally expanding direction converts itself into a contracting direction, causing an excursion away from the reflecting barrier. The finite exponent values go far away from zero and a breakdown in the shadowing occurs. The times between these breakdowns (or glitches) are analogous to first passage times of the shadowing distance to approach the order of the invariant distribution length in phase space. The invariant distribution can be an attractor in the case of chaotic non-conservative systems.

3 METHODOLOGY

Here we discuss some issues that affect the computation of the finite-time Lyapunov exponents and their distributions, and in consequence, the computation of the predictability index. The predictability index depends on the calculated distributions, which in turn depend on the initial orientation of the deviation vectors, the choice of the finite-time interval sizes and the total integration time during which the finite-intervals are accumulated.

The finite-time Lyapunov exponents reflect the growth rate of the orthogonal semiaxes (equivalent to the initial deviation vectors) of one ellipse centred at the initial position. These axes change their orientation and length as the orbit is integrated during a given finite-time Δt, following equation (2). Each initial orientation will lead to different exponents (Ziehmann, Smith & Kurths 2000). One option is to have the axes pointing to the local expanding/contracting directions, given by the eigenvectors. Then, at local time-scales, the eigenvalues will provide insight on the stability of the point. Another option is to start with the axes pointing to the direction which may have grown the most under the linearized dynamics. Yet another choice is pointing them to the globally fastest growth direction. In this work, we have preferred, as initial axes of the ellipse, a set of

orthogonal vectors randomly oriented, following Vallejo, Viana & Sanjuan (2008). We have made this choice because, as there is no initial preferred orientation, the evolution of the deviation vectors is a direct consequence of the flow time-scales.

The key factor to build the finite-time distributions is finding the most adequate Δt, to be large enough to ensure a satisfactory reduction of the fluctuations, but small enough to reveal slow trends. This length is different for every orbit. So, in principle, one needs to calculate the distributions for a variety of finite intervals lengths and observe the progressive evolution of the distribution shapes. If one uses the smallest intervals, the deviation vectors will trace the very local flow dynamics. As one selects larger intervals, the local regime of the flow is replaced by the global dynamics regime, and the vectors are oriented depending on the global properties of the flow, including any transient behaviour. Finally, with the largest interval lengths, the vectors are oriented towards the final asymptotic directions of the flow, when the dynamics reaches the final invariant state.

In addition to the choice of the finite interval length and the initial directions of the axes, the total integration time used to compute the distribution is also of importance (Vallejo et al. 2003). Because the integration time for gathering the finite-time exponents is also finite, the distributions may just reflect any transient state of the system during such integration period, instead of reflecting the global or final stationary state. For instance, a common phenomenon found in conservative systems is the existence of stickiness or trapped motions. A chaotic orbit may be confined to a torus for a while, but after a very long time, it leaves the confinement and again shows the chaotic behaviour.

Another factor to take into account is the fact that we analyse Hamiltonian conservative systems. The random walker model described above was derived for dissipative system, using orbits located in the basin of attraction and selecting the interval lengths leading to Gaussian distributions (Sauer et al. 1997). There are no attractors in Hamiltonian systems, and we aim to check the applicability of this model to conservative systems. To do this, we will sample different finite-time intervals lengths Δt searching for changes in the shape of the distributions, as an estimator of reaching the proper time-scale.

Our previous results (Vallejo et al. 2008) show that when using the very smallest interval lengths, similar to the integration step, the distributions show many peaks, because the randomly oriented deviation vectors are not able to evolve during such very small intervals. When the finite-time intervals are slightly larger, the resulting finite-time exponent distributions begin to be similar to flat uniform distributions. The finite-time exponents cannot be regarded at these time-scales as similar to random variables leading to Gaussian distributions, as the deviation vectors have been allowed to evolve from the initially randomly selected deviation directions, but they had not enough time to tend to the finally fastest growing directions. These distributions are then characterized by large negative kurtosis. Finally, when the finite intervals are larger, the deviation vectors are oriented to the globally fastest growth direction, that may, or may not be, the final asymptotic behaviour. This asymptotic direction is only reached at very long (infinite) intervals.

This work focuses on detecting the finite-time interval lengths when the change from the local to the global regime occurs. The Poincaré crossing time with the surface of section is a good estimator of these time-scales, but unless the orbit is periodic, this crossing time depends on the selection of the surface of section. Indeed, it is not constant in the phase space once the surface has been selected.

Another good estimator for detecting this behaviour change is the kurtosis values of the finite-time distributions. These values evolve from zero to positive values, as a consequence of the shape changes when the finite-time exponents leave the local flow dynamics and tend towards the global regime. The larger the positive kurtosis values, the more peaked the distributions will be.

Finally, one observes the asymptotic regime of the flow at the time-scales when the mean of the distributions begins to be centred around the final asymptotic value (Vallejo et al. 2003). As mentioned before, the flow may experience several transient periods before reaching this final asymptotic state.

The scaling formula equation (3) is an asymptotic formula, true when $\delta \to 0$ and to the extent that one finite-time exponent is closer to zero than all the others. When two or more finite-time exponents are equally distant to zero, the applicability of this scaling formula is not established (Sauer 2002). In this work we analyse if the biased random walker model, from which this equation derives, is valid even when there are two or more exponents close to zero, as happens in Hamiltonian flows. In a general dynamical system, there is at least one asymptotic Lyapunov exponent tending to zero, as there is always one neutral direction in the flow. But in N-dimensional Hamiltonians, because of their conservative nature, two exponents are at least close to zero, because the Lyapunov exponents follow the pairing property $\lambda_i = -\lambda_{N-i}$ for ($i = 1, 2, \ldots, N-1$). Moreover, if we deal with quasi-periodic orbits or irregular, yet not chaotic, orbits, additional exponents will be zero.

We will identify the closest to zero exponent by calculating the finite-time exponents distributions for all available exponents, and selecting as closest to zero the exponent corresponding to the distribution whose mean is closest to zero. This technique has been successfully applied to dissipative systems in Vallejo & Sanjuan (2013). The results show that the closer to zero the mean of the distribution is, the stronger the detection of fluctuations around zero. These fluctuations are in turn a good indicator of the non-hyperbolic nature, low predictability, of the orbit. The strength of the fluctuations can be derived from the computation of the probability of positivity P_+ of the distributions.

The time-scales, when the changes from the local to global behaviour are detected, can be shorter than the time-scales when asymptotic behaviour is reached and the mean of the distribution tends to the asymptotic infinite zero value. This implies that when the finite-intervals are not large enough to reach the asymptotic regime, we may still detect changes due to entering in the global regime and get insight into the predictability of the orbit. This may happen even when the mean will still not be close to zero, and the fluctuations around zero will be hardly detected.

Massless particles subject to the selected gravitational potentials are integrated using a standard variational method to compute the finite-time Lyapunov exponents. We solve at the same time the flow equations and the fundamental equations or evolution of the distortion tensor, associated with the initial set of deviation vectors used for the exponents computation. Here we raise a final note concerning the selection of the integrator. Standard integrators may be thought as quantitatively accurate, but not qualitatively, since small errors may not conserve the energy, contrary to a symplectic scheme. However, selecting a given symplectic scheme is not as straightforward as one might think. Energy conservation is not always the invariant that must be preserved (it may be the angular moment first integral), and integrable Hamiltonians approximated by symplectic schemes may manifest apparent chaos (Newman & Lee 2005). Indeed, the only integrator which preserves all invariants has been proved to be the true solution itself (Stuchi 2002).

As a consequence, we have used as integrator the well known and robust Dop853 algorithm described in Hairer, Norsett & Wanner (1993). We have checked the Lyapunov exponents to follow the pairing property and the energy value to be constant throughout the computation, typically being within a percentual error of 10^{-11} for meridional potentials and 10^{-8} for the Milky Way potentials.

4 PREDICTABILITY IN MERIDIONAL POTENTIALS

In this section we compute the predictability index as derived from equation (3) in simple two degrees-of-freedom (d.o.f.) potentials. We will check if the subjacent diffusion model origin is valid in these conservative systems, where several asymptotic exponents are zero.

Meridional plane potentials are those of the form $V(x, y) = V(R, z)$, being R and z the cylindrical coordinates, corresponding to an axisymmetric galaxy (Binney & Tremaine 1987). These are relatively simple potentials that can show complex behaviours, which are found in more realistic galactic-type potentials.

The motion in the meridional plane can be described by an effective potential:

$$V_{\text{eff}}(R, z) = V(R, z) + \frac{L_z^2}{2R^2}, \tag{4}$$

where R and z are the cylindrical coordinates. For each orbit, the energy $E = E(x, y, v_x, v_y)$ is an integral of motion. Once E is fixed, only three of the four coordinates are independent and define the initial condition for the integrator.

If the energy E and the z-component of the angular momentum L_z are the only two isolating integrals, an orbit would visit all points within the zero-velocity curve, defined as $E = V_{\text{eff}}$. Sometimes, there are limiting surfaces that forbid the orbit to fill this volume, implying the existence of a third integral of motion, whose form cannot be explicitly written. In this case, the particle is confined to a 3 torus. Alternatively, there are some axisymmetric potentials where the orbits can indeed fill the meridional plane. These are irregular (or ergodic) orbits which are only limited by two integrals of motion.

4.1 Hénon–Heiles system

The Hénon–Heiles system was one of the first models used to show how a very simple system possesses highly complicated dynamics (Hénon & Heiles 1964). It contains two, properly weighted, coupling terms, x^2y and y^3, leading to a Hamiltonian with a $2\pi/3$ rotation symmetry and three exits in the potential well for energy values above the critical energy:

$$H = \frac{1}{2}\left(p_x^2 + p_y^2\right) + \frac{1}{2}\left(x^2 + y^2 + 2x^2y + \frac{2}{3}y^3\right). \tag{5}$$

We have selected four initial conditions leading to four prototypical behaviours in this system. These orbits can be seen in Fig. 1, and their corresponding initial conditions are listed in Table 1. The first analysed case is the orbit labelled as H1. The Poincaré section is depicted in Fig. 2 (left). This orbit is a weakly chaotic orbit with $\lambda = 0.015$. When considering the crosses of the $x = 0$ plane with $v_x > 0$, the averaged Poincaré section crossing time is $T_{\text{cross}} = 13.0$, with a minimum value of 10.1. When considering the crosses of the $y = 0$ plane with $v_y > 0$, the averaged Poincaré section crossing time is $T_{\text{cross}} = 16.5$, with a minimum value of 12.4. These
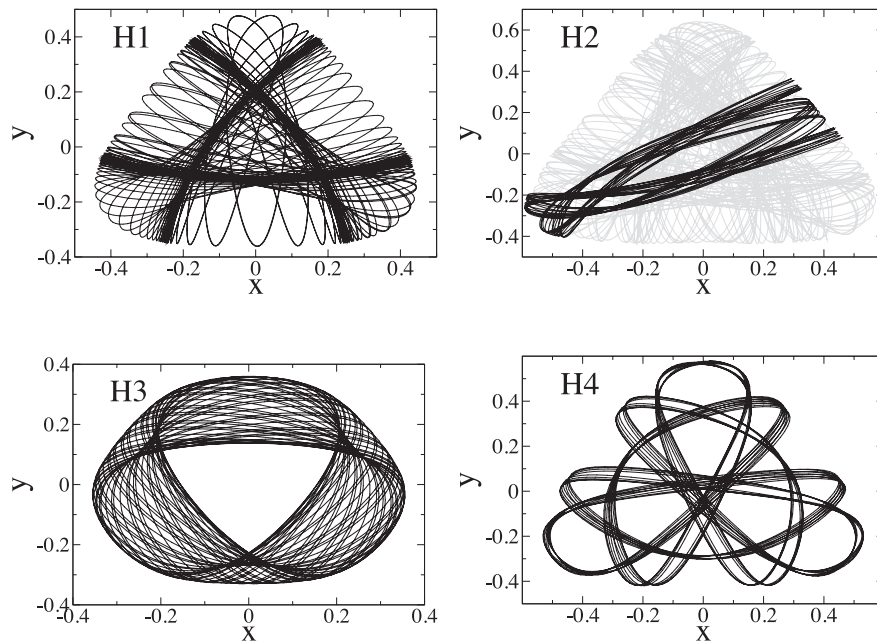
Figure 1. Four orbits selected for calculating their predictability in the Hénon–Heiles system. The corresponding initial conditions are listed in Table 1. Upper left: H1, a weakly orbit with asymptotic Lyapunov exponent $\lambda = 0.015$. Upper right: H2, a sticky, chaotic asymptotically, orbit with asymptotic Lyapunov exponent $\lambda = 0.046$. The points with a regular-like transient period $t < 4000$ are plotted in darker colour. Bottom left: H3, a regular orbit, linked to a period 1 orbit, with asymptotic Lyapunov exponent $\lambda = 0.0$. Bottom right: H4, a regular orbit, linked to a period 5 orbit, with asymptotic Lyapunov exponent $\lambda = 0.0$.

Table 1. Selected orbits for two 2 d.o.f. meridional potentials systems, Hénon–Heiles and Contopoulos, and for one 3 d.o.f. Milky Way system.

| System	Orbit	d.o.f.	Initial condition	Control parameter
Hénon–Heiles	H1	2	$x = 0.000000, y = -0.119400, v_x = 0.388937, E = 1/12$	–
Hénon–Heiles	H2	2	$x = 0.000000, y = 0.095000, v_x = 0.396503, E = 1/8$	–
Hénon–Heiles	H3	2	$x = 0.000000, y = 0.137500, v_x = 0.386627, E = 1/12$	–
Hénon–Heiles	H4	2	$x = 0.000000, y = -0.031900, v_x = 0.307044, E = 1/8$	–
Contopoulos	C1	2	$x = 0.03744, y = 0.0, v_x = 0.0480, E = 0.00765$	$\epsilon = 4.4$
Contopoulos	C2	2	$x = 0.03744, y = 0.0, v_x = 0.0480, E = 0.00765$	$\epsilon = 4.5$
Milky Way	M1	3	$x = 10.0, y = 0.0, z = 0.0, v_x = 0.0, v_y = 200.0, v_z = 0.0$	$\phi_{halo} = 0.0$
Milky Way	M2	3	$x = 10.0, y = 0.0, z = 10.0, v_x = 0.0, v_y = 45.0, v_z = 0.0$	$\phi_{halo} = 0.0$
Milky Way	M3	3	$x = 10.0, y = 0.0, z = 10.0, v_x = 0.0, v_y = 200.0, v_z = 0.0$	$\phi_{halo} = 90.0$
Milky Way	M4	3	$x = 5.0, y = 0.0, z = 0.5, v_x = 0.0, v_y = 100.0, v_z = 0.0$	$\phi_{halo} = 0.0$
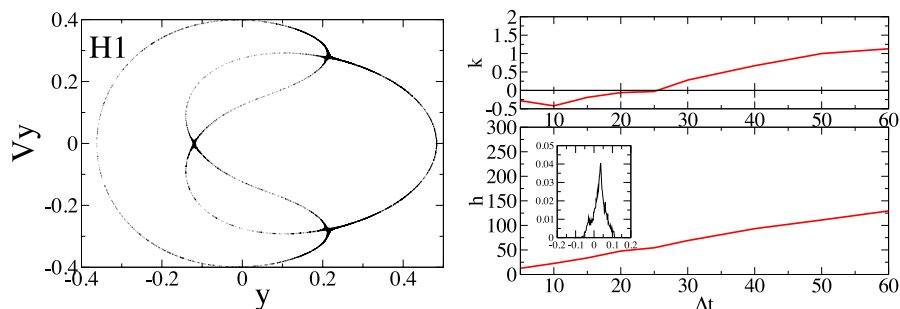
Figure 2. Hénon–Heiles weakly chaotic orbit H1. Left: Poincaré section y–v_y with plane $x = 0$ and $v_x > 0$. Right: evolution of the kurtosis k and predictability index h of the finite-time exponents distributions as the finite-time length is increased. Inset: finite-time exponents distribution for $\Delta t = 25.1$. The predictability index is $h = 54.0$.

time-scales roughly indicate the change of behaviour of the finite-time distributions as the finite-time intervals grow.

In Fig. 2 (right) we have plotted the hyperbolicity index derived from the closest to zero exponent distributions and the corresponding kurtosis values, against a variety of increasing finite interval lengths Δt. The total integration time used to build the distributions is $T = 10^5$ when $\Delta t < 50.0$ and $T = 10^6$ for larger intervals sizes.
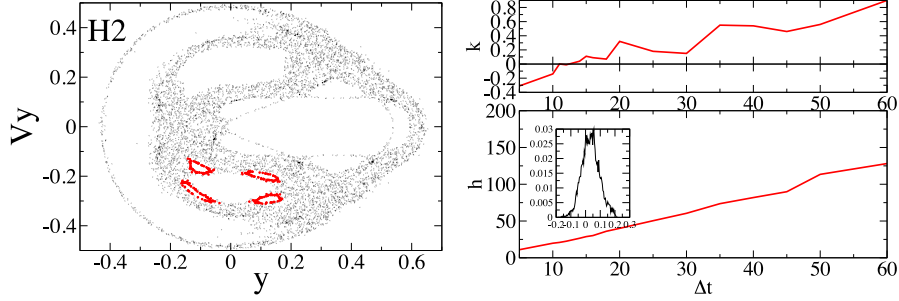
Figure 3. Hénon–Heiles sticky, chaotic asymptotically orbit H2. Left: Poincaré section y–v_y with plane $x = 0$ and $v_x > 0$. A regular-like transient period $t < 4000$ is overplot with darker colour. Right: evolution of the kurtosis k and predictability index h of the finite-time exponents distributions as the finite-time length is increased. Inset: finite-time exponents distribution for $\Delta t = 11.0$. The predictability index is $h = 20.9$.

There is a clear trend of increasing h values as the interval size is larger. The kurtosis shows a similar evolution from the most negative values towards the positive ones. The kurtosis curve crosses the zero value at $\Delta t = 25.1$. The corresponding finite-time Lyapunov exponents distribution of the closest to zero exponent for this interval size is seen in the inset of the figure. It is characterized by a mean $m = 0.03$ and a probability of positivity $F_+ = 0.8$. The Δt is large enough to allow the deviation vectors to enter in the global regime of the flow, but is not large enough to reach the asymptotic zero value. Regardless of the above, some oscillations around zero are already detected and these oscillations can be considered a good indicator of the non-hyperbolicity of the flow. The predictability index derived from this distribution is $h = 54.4$. We note here that because of the small slope of the kurtosis and predictability curves, small changes of the estimation of the interval size do not lead to large variations in the predictability estimation.

The second analysed case is the orbit labelled as H2 in Fig. 1 and Table 1. The corresponding Poincaré section is depicted in Fig. 3 (left). This is a chaotic orbit with $\lambda = 0.046$. Considering the crosses of the $x = 0$ plane with $v_x > 0$, the averaged Poincaré section crossing time is $T_{\mathrm{cross}} = 13.4$, with a minimum value of 8.9. When considering the crosses of the $y = 0$ plane with $v_y > 0$, the averaged Poincaré section crossing time is $T_{\mathrm{cross}} = 14.5$, with a minimum value of 7.5.

In Fig. 3 (right) we observe the trend of increasing kurtosis with Δt. The kurtosis zero-cross is found at $\Delta t = 11.0$. The corresponding closest to zero exponent finite-time distribution is seen in the inset of the figure. It is characterized by a mean $m = 0.04$ and a probability of positivity $F_+ = 0.7$. The derived predictability index is $h = 20.9$. This is a worse predictability value than the previous case, yet similar in order of magnitude. We may conclude that the

shadowing time-scales are similar in both cases. As both orbits have positive λ values, they are chaotic, yet predictable.

We have seen that orbit H1 has a relatively small Lyapunov exponent, so a relatively long Lyapunov time. This is a prototypical behaviour for a particle being chaotic, but confined to a certain region of the available phase space. But there are chaotic orbits with positive Lyapunov exponent values that show regular-like appearance during certain transient periods. These orbits stick during these transients close to islands of stability before entering in the big chaotic sea. These periods can sometimes be very short, sometimes very long. These orbits are called sticky orbits, or confined orbits (Athanassoula et al. 2010), because they generate confined structures in the configuration space.

The sticky, chaotic asymptotically, orbit H2 presents one regular-like transient during the first 4000 time units. The Poincaré section corresponding to this period is seen in Fig. 4 (left). Considering the crosses of the $x = 0$ plane with $v_x > 0$, the averaged Poincaré section crossing time is $T_{\mathrm{cross}} = 14.6$, with a minimum value of 13.8. When considering the crosses of the $y = 0$ plane with $v_y > 0$, the averaged Poincaré section crossing time is also $T_{\mathrm{cross}} = 14.6$, with a minimum value of 13.2.

In Fig. 4 (right) we observe the trend of increasing kurtosis with Δt. The kurtosis zero-cross is found at $\Delta t = 19.1$. The corresponding closest to zero exponent finite-time distribution is seen in the inset of the figure. It is characterized by a mean $m = -0.01$ and a probability of positivity $F_+ = 0.28$. The derived predictability index is $h = 31.7$. This means a higher predictability during the regular-like transient when compared with the predictability value resulting from integrating beyond the transient lifetime. However, this value is lower than the value of the chaotic orbit H1. This is sourced to the selection of one of the lowest values of the available ones during

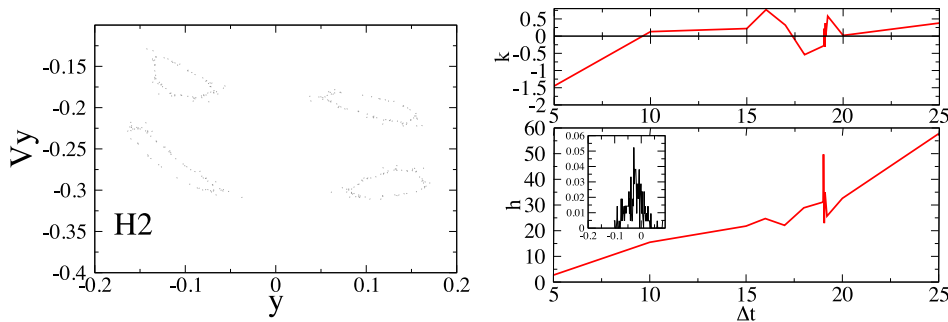**Figure 4.** Regular-like period of the Hénon–Heiles chaotic orbit H2. The figure shows the points under the regular-like transient period $t < 4000$. Left: Poincaré section y–v_y with plane $x = 0$ and $v_x > 0$. Right: evolution of the kurtosis k and predictability index h of the finite-time exponents distributions as the finite-time length is increased. Inset: finite-time exponents distribution for $\Delta t = 19.1$. The predictability index is $h = 31.7$.
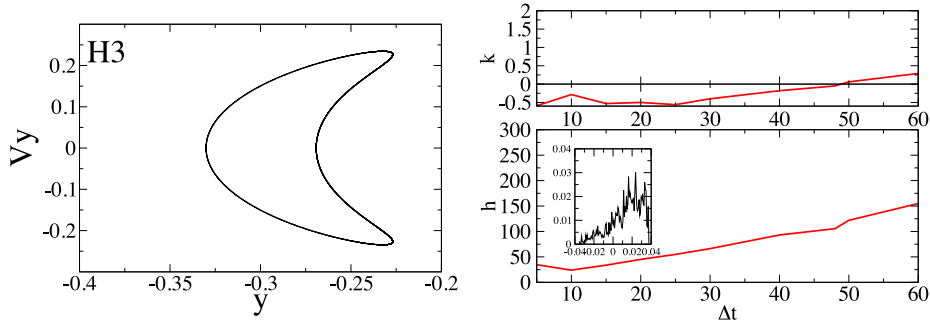
Figure 5. Hénon–Heiles regular orbit H3. Left: Poincaré section y–v_y with plane $x = 0$ and $v_x > 0$. Right: evolution of the kurtosis k and predictability index h of the finite-time exponents distributions as the finite-time length is increased. Inset: finite-time exponents distribution for $\Delta t = 48.3$. The predictability index is $h = 105.5$.
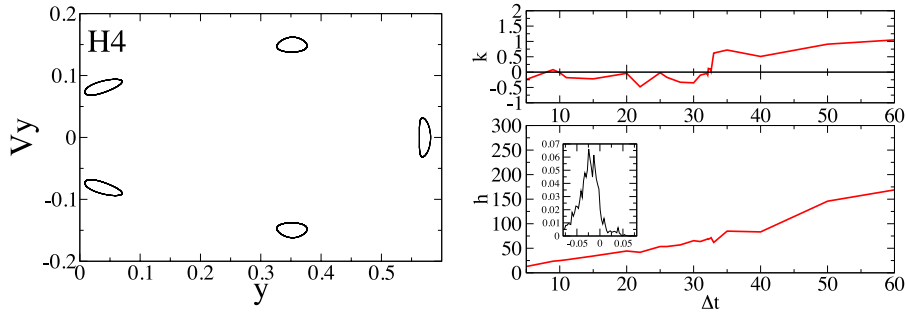

Figure 6. Hénon–Heiles regular orbit H4. Left: Poincaré section y–v_y with plane $x = 0$ and $v_x > 0$. Right: evolution of the kurtosis k and predictability index h of the finite-time exponents distributions as the finite-time length is increased. Inset: finite-time exponents distribution for $\Delta t = 32.1$. The predictability index is $h = 69.2$.

the distribution shape transition, where the h-index values suffer several oscillations, as seen in Fig. 4 (right). But it is also sourced to the nature of the transient, that, being regular in appearance, it is not a truly regular motion.

The third analysed case is the orbit labelled as H3 in Fig. 1 and Table 1. We have chosen this orbit because we want to analyse the applicability of the power law to orbits with zero Lyapunov exponents in addition to the obvious two central trivially zero exponents. This is a regular orbit with $\lambda = 0.0$, where all exponents are zero because the Hénon–Heiles system is a 2 d.o.f. Hamiltonian system.

The corresponding Poincaré section is depicted in Fig. 5 (left). Considering the crosses of the $x = 0$ plane with $v_x > 0$, the averaged Poincaré section crossing time is $T_{\text{cross}} = 12.4$, with a minimum value of 11.6. When considering the crosses of the $y = 0$ plane with $v_y > 0$, the averaged Poincaré section crossing time is $T_{\text{cross}} = 12.4$, with a minimum value of 11.7.

The evolution of the predictability index h with the interval size is shown in Fig. 5 (right). The kurtosis shows the previous trend from the most negative values towards the positive ones. The zero crossing is found at $\Delta t = 48.3$. The corresponding distribution of the closest to zero exponent is plotted in the inset of the figure. It is characterized by a mean $m = 0.01$ and a probability of positivity $F_+ = 0.8$. The derived h predictability index value is higher than the previous cases, $h = 105.5$.

When one compares the predictability of this orbit with the previous cases, the obtained predictability index h is one order of magnitude larger. The biased random walk seems to be applicable to the final invariant state, even when the finite-time exponents distributions of regular orbits do not follow a normal distribution shape. This means that the test particle sometimes approaches the real orbit, having the machine precision as bias, in the contracting

directions, and sometimes moves farther away from the real orbit in the expanding directions.

The fourth analysed case in the Hénon–Heiles system is the orbit labelled as H4 in Fig. 1 and Table 1. This is a regular orbit with $\lambda = 0.0$, associated with a fifth-periodic orbit. The corresponding Poincaré section is depicted in Fig. 6 (left). Considering the crosses of the $x = 0$ plane with $v_x > 0$, the averaged Poincaré section crossing time is $T_{\text{cross}} = 12.9$, with a minimum value of 12.3. When considering the crosses of the $y = 0$ plane with $v_y > 0$, the averaged Poincaré section crossing time is $T_{\text{cross}} = 12.9$, with a minimum value of 9.7.

The evolution of the predictability index h with the interval size is shown in Fig. 6 (right). The previous evolution of the kurtosis from negative to positive values is observed. The kurtosis zero-cross is observed at $\Delta t = 32.1$.[1] The corresponding closest to zero exponent distribution is plotted in the inset of the figure. It is characterized by a mean $m = -0.02$ and a probability of positivity $F_+ = 0.2$. Because of the Hamiltonian exponents pairing properties, the results are equivalent except for the reversed signs to the previously discussed cases.

The derived predictability index is $h = 69.2$. The predictability index is in agreement with the previous cases, with a better predictability index than the chaotic cases but a worse h index than the M3, regular orbit case.

---

[1] We see another zero crossing at around $\Delta t = 9.0$. This value is slightly below the T_{cross} range of values. But as Δt increases, the distribution returns to a flat shape again. As a consequence, the peaks are sourced to still be in the local regime.

4.2 Contopoulos system

We will apply our method to analyse orbits that behave in appearance like regular orbits, but that are $\lambda > 0$ chaotic. These orbits are found in the following system:

$$H = \frac{1}{2}\left(p_x^2 + p_y^2\right) + \frac{1}{2}(Ax^2 + By^2) - \epsilon xy^2. \qquad (6)$$

This model was originally studied by Contopoulos (1970) and it provides a rich dynamical behaviour despite its simplicity. It can be seen as a simpler version of the Hénon–Heiles with just one mixed higher order term, xy^2, which introduces the essential non-linearity of the problem. Conversely to the Hénon–Heiles, this potential has a y-axis symmetry and only two exits.

The fixed model parameters are the amplitude parameters $A = 1.6$ and $B = 0.9$. These values are chosen to be near the resonance $\sqrt{A/B} = 4/3$, as in Contopoulos (1970). The initial condition will be the same in all cases, $x = 0.03744$, $y = 0$, $v_x = 0.0480$, and the energy value is $E = 0.00765$. The control parameter is the coupling parameter ϵ.

The first case that we have considered is when we fix the control parameter $\epsilon = 4.4$. This is the orbit labelled as C1 in Fig. 7 and Table 1. The Poincaré section $x–v_x$ with plane $y = 0$ is seen in Fig. 8 (left). This is a regular in appearance, very thin chaotic strip, with $\lambda = 0.093$. When considering the crosses of the $x = 0$ plane with $v_x > 0$, the averaged Poincaré section crossing time is $T_{\text{cross}} = 13.8$, with a minimum value of 6.0. When considering the crosses of the $y = 0$ plane with $v_y > 0$, the averaged Poincaré section crossing time is $T_{\text{cross}} = 14.2$, with a minimum value of 13.9.

The evolution of the predictability index h with the interval size is shown in Fig. 8 (right), where the evolution of the kurtosis from negative to positive values can be seen. The kurtosis zero-cross is

found at $\Delta t = 13.9$. The corresponding closest to zero exponent distribution is plotted in the inset of the figure. It is characterized by a mean $m = -0.01$ and a probability of positivity $F_+ = 0.3$. The derived predictability index is $h = 24.2$. The predictability index is in agreement with the previous cases and this value is very similar to the predictability of the chaotic cases of the Hénon–Heiles system, confirming the lower predictability of the 'regular' in appearance, chaotic orbit.

The second case analyses the same initial condition fixing $\epsilon = 4.5$. This is the orbit labelled as C2 in Fig. 7 and Table 1. The Poincaré section $x–v_x$ with plane $y = 0$ is seen in Fig. 9 (left). This is a weakly chaotic orbit with $\lambda = 0.0125$. This orbit is very close to a periodic orbit, meaning an averaged Poincaré section crossing time $T_{\text{cross}} = 14.5$, both for crosses of the $x = 0$ plane with $v_x > 0$, and also when considering the crosses of the $y = 0$ plane with $v_y > 0$.

The evolution of the predictability index h with the interval size is shown in Fig. 9 (right). The kurtosis zero-cross in the evolution of the kurtosis from negative to positive values is found at $\Delta t = 17.15$. The corresponding closest to zero exponent distribution is plotted in the inset of the figure. It is characterized by a mean $m = -0.003$ and a probability of positivity $F_+ = 0.4$. The values of the mean and F_+ reflect that the asymptotic behaviour has already been reached at these time-scales with contracting and expanding oscillations around zero of equal likelihood.

The figure shows strong oscillations in the predictability curve h against Δt. These oscillations are linked to the presence of peaks in the distributions and the non-ergodic nature of the orbit. These oscillations make the h index have strong variations with Δt, but even with these oscillations, the interval belonging to the kurtosis zero-cross is seen. The predictability index as computed from the selected Δt is then $h = 11.9$. This predictability index is in agreement
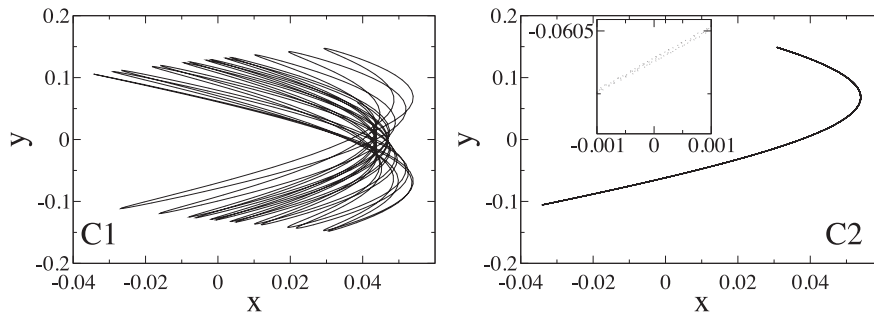

Figure 7. Two orbits selected for calculating their predictability in the Contopoulos system. The initial condition and the values of the control parameter ϵ are listed in Table 1. Left: C1, a chaotic orbit with asymptotic Lyapunov exponent $\lambda = 0.093$. Right: C2, a weakly chaotic orbit that, in appearance, is a periodic orbit. It must be zoomed in to reflect its chaotic nature. The asymptotic Lyapunov exponent $\lambda = 0.0125$.
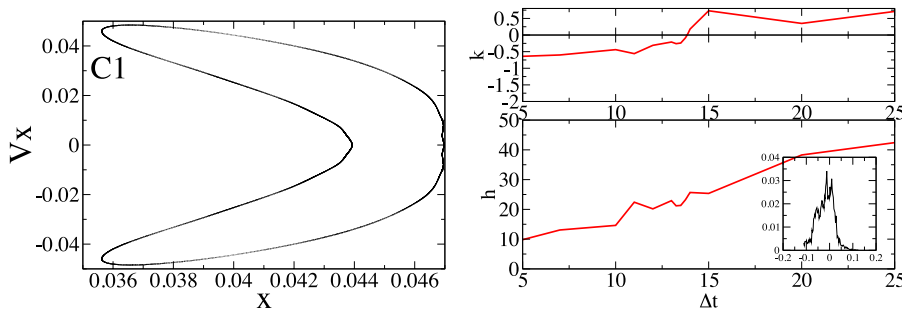

Figure 8. Contopoulos chaotic orbit C1. Left: Poincaré sections $x–v_x$ with plane $y = 0$ and $v_y > 0$. Right: evolution of the kurtosis k and predictability index h of the finite-time exponents distributions as the finite-time length is increased. Inset: finite-time exponents distribution for $\Delta t = 13.9$. The predictability index is $h = 24.2$.
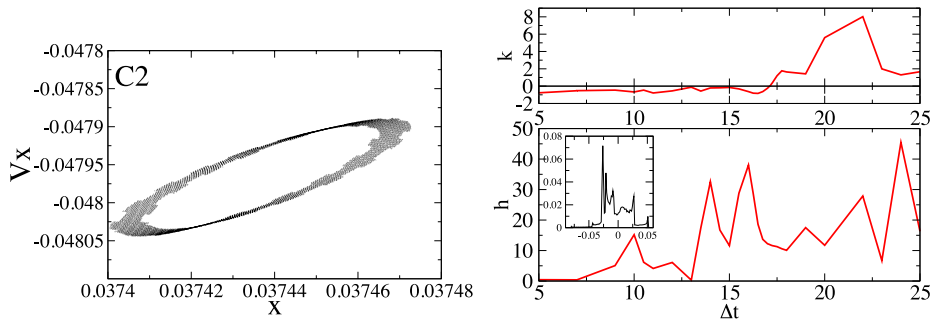
Figure 9. Contopoulos weakly chaotic orbit C2. Left: Poincaré sections x–v_x with plane $y = 0$ and $v_y > 0$. Right: evolution of the kurtosis k and predictability index h of the finite-time exponents distributions as the finite-time length is increased. Inset: finite-time exponents distribution for $\Delta t = 17.15$. The predictability index is $h = 11.9$.

with the previous cases. This value means a lower predictability in this case than previous chaotic cases.

5 PREDICTABILITY IN A MILKY WAY-TYPE POTENTIAL

In this section we show how the predictability index behaves when applied to a more realistic galactic potential. There is a considerable number of realistic galactic models in the literature that capture and describe several observed features such as bars, spirals or rings. See, among others, Pfenniger (1984), Skokos, Patsis & Athanassoula (2002), Wang et al. (2012) and Contopoulos & Harsoula (2013). In this paper, we have selected the potential described in Law, Majewski & Johnston (2009) and references therein. This is a smooth fixed gravitational time-independent potential that models the Milky Way, but focus on the parameters controlling the shape and orientation of a triaxial dark halo. It consists of a Miyamoto–Nagai disc (Miyamoto & Nagai 1975), a Hernquist spheroid and a logarithmic halo.

This potential is more realistic than the previously presented models. It reproduces the flat rotation curve for a Milky-Way-type galaxy and it can be easily shaped to the axial ratios of the ellipsoidal isopotential surfaces.

We will analyse the four orbits shown in Fig. 10, labelled as M1, M2, M3 and M4. The first orbit, M1, is a regular orbit, selected for comparing the time-scales of this model with the previously analysed meridional potentials. The following orbits, M2, M3 and M4, are chaotic orbits. These are confined within some phase-space domain for a while, but, afterwards, can escape from those domains. As a consequence of these transients, the distributions shapes vary depending on the selection of the finite-time lengths.

In systems with 2 or less d.o.f., regular and non-regular orbits are separated by impenetrable barriers, the Kolmogorov–Arnold–Moser (KAM)-tori, leading to islands of regularity embedded into a surrounding chaotic sea. According to the KAM theorem, these tori will survive under small perturbations if their frequencies are sufficiently incommensurable (Lichtenberg & Lieberman 1992). Resonant tori may be strongly deformed even under small perturbations, however, leading to a complicated phase-space structure of interleaved regular and chaotic regions. Where tori persist, the motion can still be characterized in terms of N local integrals. Where tori are destroyed, the motion is chaotic and the orbits move in a space of higher dimensionality than N.

In systems with more than 2 d.o.f., like the selected potential, the chaotic sea contains a hidden non-uniformity because the motion can diffuse through invariant tori, reaching arbitrarily far regions.

Within the chaotic sea there are cantori, leaking or fractured KAM-tori, associated with the breakdown of integrability. These cantori are just partial barriers, which over short times, divide the chaotic orbits into two types: confined and non-confined. The confined ones are chaotic orbits which are trapped near the regular islands and, for a while, exhibit regular-like behaviour. Conversely, the unconfined orbits travel unmixed through the whole allowed sea. Furthermore, the cantori are partial barriers, allowing one orbit to change from one class to the other, via the intrinsic diffusion or Arnold diffusion. This is a very slow phenomenon, with typical time-scales longer than the age of the Universe. In six-dimensional phase-space systems, the sticky transients are not present, cantori appears, and the Arnold diffusion produces the ultimate merging of all orbits. But this diffusion seems to be very small. Strong local instability does not mean diffusion in phase space. And some chaotic trajectories may require very long time-scales to reveal its asymptotic nature. These trajectories can have very short Lyapunov times but they cannot show the expected significant orbital changes but at long times (Tsiganis, Varvoglis & Hadjidemetriou 2002; Cincotta & Giordano 2008; Cachucho, Cincotta & Ferraz-Mello 2010). In these cases, the dynamics can be considered as regular motion from an astronomical point of view during the applicable time-scales.

As a consequence, the fact that two regions in phase space are connected, does not mean that all the areas in that volume will be accessed on comparable time-scales. This long lifetime transient, unconfined orbit, is sometimes called near-invariant distribution, as it uniformly populates the filling region. It is remarkable that even when the true equilibrium corresponds to a uniform distribution through both cavities, at physically meaningful time-scales, the quasi-equilibrium may have one cavity uniformly populated while the other one is, essentially, empty.

The dynamical system to solve is a particle (star) subject to a potential built upon three components: $V = \Phi_{\text{disc}} + \Phi_{\text{sphere}} + \Phi_{\text{halo}}$. The respective contribution of every component to the gravitational potential is given by

$$\Phi_{\text{disc}} = -\alpha \frac{GM_{\text{disc}}}{\sqrt{R^2 + (a + \sqrt{z^2 + b^2})^2}}, \tag{7}$$

$$\Phi_{\text{sphere}} = -\alpha \frac{GM_{\text{sphere}}}{r + c}, \tag{8}$$

$$\Phi_{\text{halo}} = v_{\text{halo}}^2 \ln\left(C_1 x^2 + C_2 y^2 + C_3 xy + (z/q_z)^2 + r_{\text{halo}}^2\right), \tag{9}$$

where the various constants C_1, C_2 and C_3 are given by

$$C_1 = \left(\frac{\cos^2 \phi}{q_1^2} + \frac{\sin^2 \phi}{q_2^2}\right), \tag{10}$$
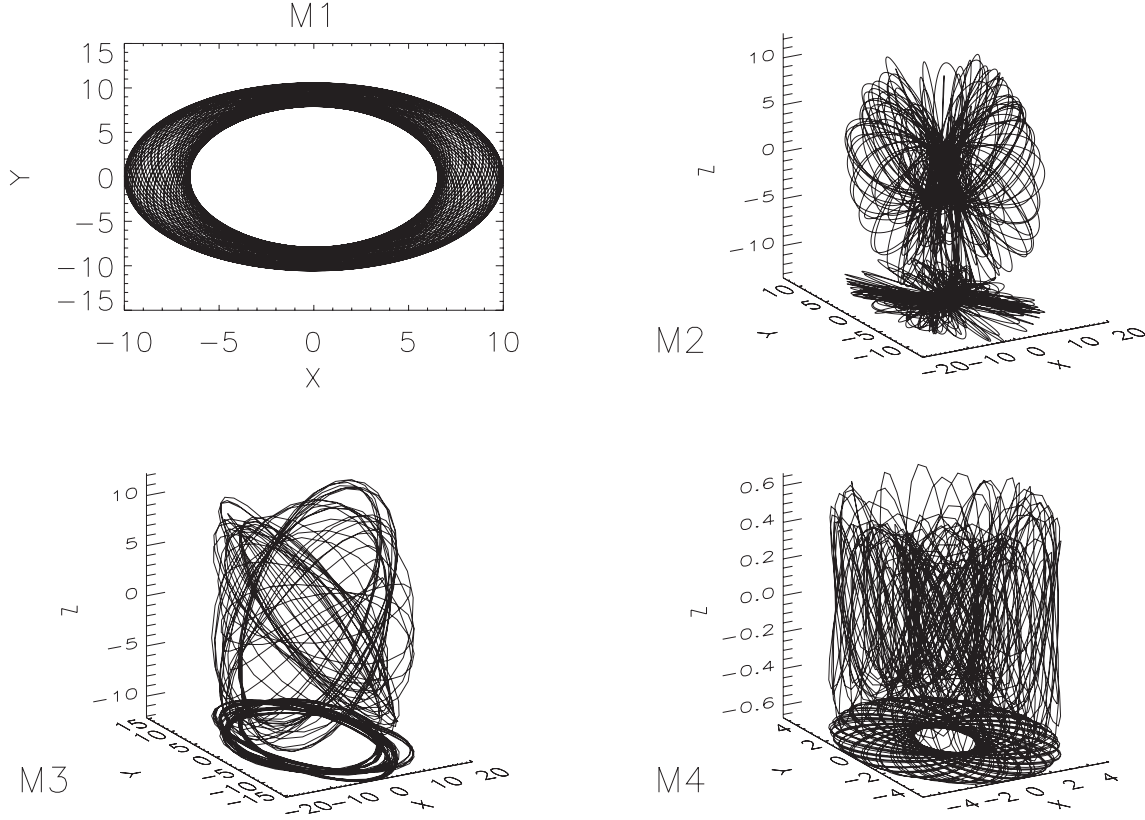
Figure 10. Four orbits selected for calculating the predictability in a Milky-Way-type potential. The initial conditions and halo orientation values are listed in Table 1. Upper left: M1, a regular orbit confined to the disc, with asymptotic Lyapunov exponent $\lambda = 0.0$. Upper right: M2, a chaotic orbit out of the disc plane, with asymptotic Lyapunov exponent $\lambda = 0.14$. Bottom left: M3, a chaotic orbit out of the disc plane, with asymptotic Lyapunov exponent $\lambda = 0.099$. Bottom right: M4, a strongly chaotic orbit, inner and close to the disc plane, with asymptotic Lyapunov exponent $\lambda = 5.86$.

$$C_2 = \left(\frac{\cos^2 \phi}{q_2^2} + \frac{\sin^2 \phi}{q_1^2} \right), \quad (11)$$

$$C_3 = 2 \sin \phi \cos \phi \left(\frac{1}{q_1^2} - \frac{1}{q_2^2} \right). \quad (12)$$

It must be noted that there is no symmetry in the potential and $V(\phi)! = V(-\phi)$ because of the sign dependency in the xy coupling factor $C3$. When $\phi = 0$, q_1 is aligned with the Galactic X-axis and equation (9) reduces to $\Phi_{halo} = v_{halo}^2 \ln ((x/q_1)^2 + (y/q_2)^2 + (z/q_z)^2 + r_{halo}^2)$. The results with $\phi = 0$ are then comparable with non-triaxial, purely logarithmic potentials. When $\phi = 90$, $q1$ is aligned with the Galactic Y-axis and it takes the role of $q2$. The parameter α could range from 0.25 up to 1.0, and following Law et al. (2009) and Johnston, Spergel & Hernquist (1995), is fixed to 1.0. We also adopt $M_{disc} = 1.0 \times 10^{11} \, M_\odot$, $M_{sphere} = 3.4 \times 10^{10} \, M_\odot$, $\alpha = 1.0$, $a = 6.5$ kpc, $b = 0.26$ kpc, $c = 0.7$ kpc and $r_{halo} = 12$ kpc. We have also fixed $v_{halo} = 128$ km s^{-1} (leading to a local standard of rest, LSR, of 220 km s^{-1}). The time units are in Gyr with these parameters values.

The control parameters of this model are the orientation of the major axis of the triaxial halo ϕ and its flattening. This flattening is introduced along the three axes by the parameters q_1, q_2 and q_z. The q_z represents the flattening perpendicular to the Galactic plane, while q_1 and q_2 are free to rotate in the Galactic plane at an angle ϕ to a right-handed Galactocentric X, Y coordinate system. We follow the parameters settings of Law et al. (2009) and, without loss of generality, $q_2 = 1.0$, $q_1 = 1.4$ and $q_z = 1.25$.

Regarding the particle initial conditions, we use stars with velocities within the halo kinematics range (Casertano, Ratnatunga & Bahcalli 1990; Chiba & Beers 2001). These initial conditions, and the values of the control parameter ϕ, corresponding to the four analysed orbits, are listed in Table 1. The initial velocity vector in all cases is contained into the $z = 0$ plane, meaning $v_z = 0.0$, and is normal to the x-axis, meaning $v_x = 0.0$. We just select in every initial condition the velocity modulus, $|v| = v_y$.

The first analysed case is a regular orbit, characterized by $\lambda = 0.0$, and confined into the disc plane $z = 0$ for the whole integration. This is the orbit labelled as M1 in Fig. 10. We have selected it in order to compare the predictability time-scales in this model with respect to the meridional potentials seen before. This is of interest because a single-step error δt may have different consequences in every model, and the shadowing times for regular orbits in different models are not necessarily similar. The corresponding Poincaré section y–v_y with plane $x = 0$ is seen in Fig. 11 (left). When considering the crosses of the $x = 0$ plane with $v_x > 0$, the averaged Poincaré section crossing time is $T_{cross} = 0.50$, with a minimum value of 0.44. When considering the crosses of the $y = 0$ plane with $v_y > 0$, the averaged Poincaré section crossing time is $T_{cross} = 0.50$, with a minimum value of 0.46.

The evolution of the kurtosis and predictability index with the interval size is shown in Fig. 11 (right). Conversely to the regular orbits seen in the meridional potentials cases, the kurtosis does not show a simple trend as the interval length grows, and there is a set of different zero crossings starting around $\Delta t = 0.06$. These oscillations at small intervals lengths below the T_{cross} range of values
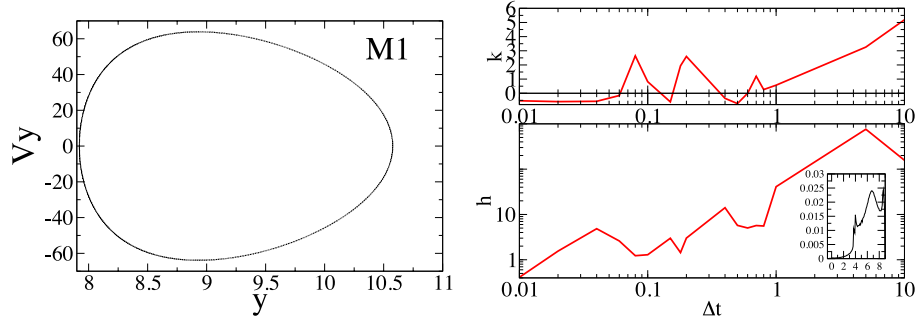
Figure 11. Milky Way regular orbit M1, confined into the disc plane, with asymptotic Lyapunov exponent $\lambda = 0.0$. Left: Poincaré sections y–v_y with plane $x = 0$ and $v_x > 0$. Right: evolution of the kurtosis k and predictability index h of the finite-time exponents distributions as the finite-time length is increased. Inset: finite-time exponents distribution for $\Delta t = 0.6$. The predictability index is $h = 5.03$.

are sourced to the fluctuations of the shapes of the distributions when the intervals are very small (Vallejo et al. 2008). The T_{cross} indicates when the global regime is reached, and the kurtosis zero-cross corresponding to these scales is seen at $\Delta t = 0.6$. The corresponding closest to zero exponent distribution is plotted in the inset of Fig. 11. It is characterized by a mean $m = 6.53$ and a probability of positivity $F_+ = 0.99$. The mean and the probability of positivity indicate that we have detected the global regime, but we are still far away from the asymptotic regime.

The predictability index is $h = 5.03$. Note that this is a very low predictability when one compares it with the values seen in the meridional potentials, both for regular and chaotic orbits. This indicates one must handle with care long integrations in this potential. The shadowing time of a regular orbit can be large or small depending on the analysed potential, because of the different dynamical times. And when the shadowing times are very low, one should use higher precision schemes, even when the gain in shadowing time may be small in the extreme cases.

The next analysed initial condition corresponds to the star labelled as M2 in Fig. 10 and Table 1. The Poincaré section y–v_y with plane $x = 0$ corresponding to this orbit is seen in Fig. 12 (left). This is a chaotic orbit characterized by $\lambda = 0.14$. We have selected this orbit because it is a chaotic orbit that initially remains in a limited domain of the phase space, but then fills up a larger domain of the available phase space, as seen in Fig. 12 (left). When considering the crosses of the $x = 0$ plane with $v_x > 0$, the averaged Poincaré section crossing time is $T_{\text{cross}} = 0.61$, with a minimum value of 0.32. When considering the crosses of the $y = 0$ plane with $v_y > 0$, the averaged Poincaré section crossing time is $T_{\text{cross}} = 0.53$, with a minimum value of 0.34. When considering the crosses of the $z = 0$

plane with $v_z > 0$, the averaged Poincaré section crossing time is $T_{\text{cross}} = 0.41$, with a minimum value of 0.04.

The evolution of the kurtosis and predictability index h with the interval size is shown in Fig. 12 (right). Conversely to previous models, there is not a simple increasing trend of kurtosis with Δt. Instead, there is a set of different zero crossings. We observe a zero crossing in the kurtosis curve at around $\Delta t = 0.035$, but this value is well below the T_{cross} range of values. There is also a zero crossing at a very large interval size (not shown in the figure), when the asymptotic regime is reached. The kurtosis zero cross corresponding to the time-scales when the global regime of the flow is reached is seen at $\Delta t = 0.6$. The corresponding closest to zero exponent distribution is plotted in the inset of the figure. It is characterized by a mean $m = -2.8$ and a probability of positivity $F_+ = 0.08$. The mean and probability of positivity indicate that we have detected the global regime, but we are still very far away from the asymptotic regime.

The predictability index is $h = 1.31$. Note that this is a very low predictability when compared with previous cases, indicating that some care must be taken when performing long integrations using this potential. Indeed, taking into account the kurtosis oscillations, we may consider that we have taken an upper limit for the value of the predictability, and within certain transients, the predictability of the orbit may be even worse.

The following initial condition is the orbit labelled as M3 in Fig. 10 and Table 1. The Poincaré section of this orbit is seen in Fig. 13 (left). This orbit is characterized by $\lambda = 0.099$. The movement is then chaotic, with some transient periods spent in the external lobes of the section. When considering the crosses of the $x = 0$ plane with $v_x > 0$, the averaged Poincaré section crossing time
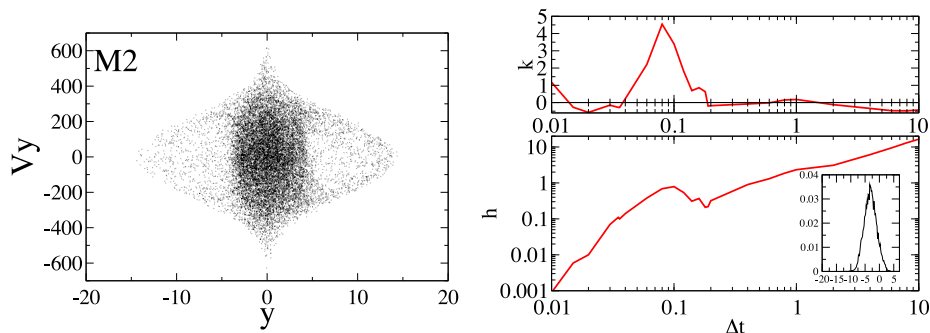
Figure 12. Milky Way chaotic orbit M2, out of the disc plane, with asymptotic Lyapunov exponent $\lambda = 0.14$. Left: Poincaré sections y–v_y with plane $x = 0$ and $v_x > 0$. Right: evolution of the kurtosis k and predictability index h of the finite-time exponents distributions as the finite-time length is increased. Inset: finite-time exponents distribution for $\Delta t = 0.6$. The predictability index is $h = 1.31$.

Figure 13. Milky Way chaotic orbit out of the disc plane, M3, with asymptotic Lyapunov exponent $\lambda = 0.099$. Left: Poincaré sections y–v_y with plane $x = 0$ and $v_x > 0$. Right: evolution of the kurtosis k and predictability index h of the finite-time exponents distributions as the finite-time length is increased. Inset: finite-time exponents distribution for $\Delta t = 1.01$. The predictability index is $h = 2.06$.
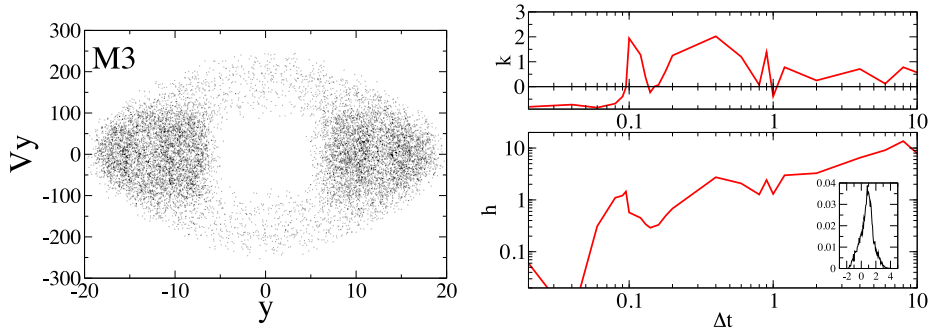
is $T_{\text{cross}} = 0.87$, with a minimum value of 0.71. When considering the crosses of the $y = 0$ plane with $v_y > 0$, the averaged Poincaré section crossing time is $T_{\text{cross}} = 0.90$, with a minimum value of 0.76. When considering the crosses of the $z = 0$ plane with $v_z > 0$, the averaged Poincaré section crossing time is $T_{\text{cross}} = 0.86$, with a minimum value of 0.62.

The evolution of the predictability index h with the interval size is shown in Fig. 13 (right). The zero crossing of the kurtosis within the range of values indicated by the Poincaré crossing time T_{cross} is found at $\Delta t = 1.01$. The corresponding finite-time distribution is plotted in the inset of the figure. It is characterized by a mean $m = 0.83$ and a probability of positivity $F_+ = 0.8$. The derived predictability index is $h = 2.06$. Similar to the previous case, we can consider this value as an upper limit to the predictability of the orbit, since the orbit may suffer transient periods with an even worse predictability.

The fourth analysed condition is the orbit labelled as M4 in Fig. 10 and Table 1. This is a star close to the disc plane, in an inner region that the previous orbits. The Poincaré section of this orbit is seen in Fig. 14 (left). This orbit is characterized by $\lambda = 5.86$. The movement is then strongly chaotic. When considering the crosses of the $x = 0$ plane with $v_x > 0$, the averaged Poincaré section crossing time is $T_{\text{cross}} = 0.18$, with a minimum value of 0.12. When considering the crosses of the $y = 0$ plane with $v_y > 0$, the averaged Poincaré section crossing time is $T_{\text{cross}} = 0.19$, with a minimum value of 0.16. When considering the crosses of the $z = 0$ plane with $v_z > 0$, the averaged Poincaré section crossing time is $T_{\text{cross}} = 0.095$, with a minimum value of 0.06.

The evolution of the predictability index h with the interval size is shown in Fig. 14 (right). The zero crossing of the kurtosis within

the range of values indicated by the Poincaré crossing time T_{cross} is found at $\Delta t = 0.07$. The corresponding finite-time distribution is plotted in the inset of the figure. It is characterized by a mean $m = -33.55$ and a probability of positivity $F_+ = 0.043$. We are again far away from the time-scales when the asymptotic dynamics is reached. The derived predictability index is $h = 0.18$. This is a very low value when compared with the previous cases, in agreement with the relatively high Lyapunov asymptotic exponent.

6 CONCLUSIONS

Our work deals with the forecast of predictability, and not with the forecast of chaoticity. Both terms are closely related, but they do not always follow the same trend. We have estimated the predictability index for a variety of prototypical orbits in several conservative galactic potentials. Contrary to other works, that focus on the *reliability* time as the inverse of the asymptotic Lyapunov exponent, thus in the chaotic, or not, nature of the orbits, we analyse the *predictability* of the system, understood as a measure of its shadowing properties.

We have seen how analysing the changes in the shapes of the distributions one can derive the predictability index. The finite-time Lyapunov exponents distributions reflect the underlying dynamics (Vallejo et al. 2003), and by using arbitrarily oriented deviation axes, one can detect varying the finite-time interval lengths, when there is a change from the local to the global, not yet asymptotic regime (Vallejo et al. 2008).

A sign of bad shadowing is the fluctuating behaviour of the closest to zero of the available Lyapunov exponents. In a general case, there can be several exponents tending to zero. Following the
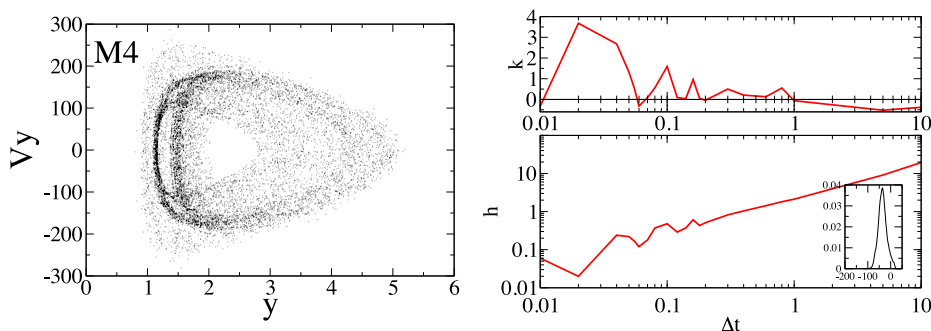

Figure 14. Milky Way strongly chaotic orbit out of the disc plane, M4, with asymptotic Lyapunov exponent $\lambda = 5.86$. Left: Poincaré sections y–v_y with plane $x = 0$ and $v_x > 0$. Right: evolution of the kurtosis k and predictability index h of the finite-time exponents distributions as the finite-time length is increased. Inset: finite-time exponents distribution for $\Delta t = 0.07$. The predictability index is $h = 0.18$.

Table 2. Predictability related parameters for the 2 d.o.f. Hénon–Heiles and Contopoulos systems, and for the 3 d.o.f. Milky Way system.

System	Orbit	Orbit type	λ	$\langle T_{\text{cross}} \rangle$	T_{min}	Δt	$h(\Delta t)$
Hénon–Heiles	H1	Weakly chaotic	0.015	14.8	10.1	25.1	54.4
Hénon–Heiles	H2	Sticky, chaotic asymptotically	0.046	13.9	7.5	11.0	20.9
Hénon–Heiles	H2($t < 4000$)	Regular-like transient	n/a	14.6	13.2	19.1	31.7
Hénon–Heiles	H3	Regular (close to period 1)	0.0	12.4	11.6	48.3	105.5
Hénon–Heiles	H4	Regular (close to period 5)	0.0	12.9	9.7	32.1	69.2
Contopoulos	C1	Chaotic	0.093	14.0	13.8	13.9	24.2
Contopoulos	C2	Weakly chaotic	0.012	14.5	14.5	17.2	11.9
Milky Way	M1	Regular	0.0	0.5	0.44	0.6	5.03
Milky Way	M2	Chaotic	0.14	0.51	0.04	0.6	1.31
Milky Way	M3	Chaotic	0.099	0.87	0.62	1.01	2.06
Milky Way	M4	Strongly chaotic	5.86	0.23	0.06	0.07	0.18

Note. λ is the asymptotic standard Lyapunov exponent. The notion *weak* or *strong* is associated with the relatively smaller or larger value of λ. $\langle T_{\text{cross}} \rangle$ is the averaged Poincaré section crossing time, and T_{min} is its minimum value. Δt is the finite-time interval length corresponding to a kurtosis zero crossing, and $h(\Delta t)$ is the corresponding predictability index.

methods presented in Vallejo & Sanjuan (2013) for a dissipative system, one should increase the finite-time interval length and select the closest to zero for deriving the predictability index. In dissipative systems the finite interval size where there is a change from local to global is the same, because all close enough orbits end in the same attractor, evolving towards similar time-scales. But in conservative systems, there are no attractors, and the finite-time lengths are specific to every orbit. In this paper, we have calculated these lengths by computing the Poincaré crossing times and detecting changes in the sign of the kurtosis of the finite-time distributions.

The results presented here are of general interest in describing how the predictability index computed using equation (3) provides information on the system dynamics. These results are summarized in Table 2. This table shows that, when calculating predictability indexes, one must take into account the time-scales of the analysed system for better interpretation of the range of values corresponding to a given model. Regarding regular orbits, we see in this table that the shadowing times can be very different when comparing regular orbits belonging to different models. This is because the consequences of a single-step error δt are different depending on the model. Regarding chaotic orbits, we see in Table 2 that the predictability indexes of chaotic orbits can be also different when they belong to different models. Two orbits can be chaotic, yet one may have a larger index than the other. The predictability index is linked to the hyperbolic nature of the orbit, and in turn, to its energy and stiffness of the system. The existence of two or more time-scales in different directions, one quickly growing, one slowly growing, can lead to stiffness, and the finite-time exponents reflect these expanding/contracting behaviours. In addition, the predictability indexes depend on the time-scales when there is a change on these behaviours, and the global regime is reached. Different energy values lead to different dynamical times, so to different time-scales.

The involvement of chaotic orbits in galactic models raises the question of the persistence of these models over the required times (Schwarzschild 1993). It is known that the mass in chaotic motion has a different distribution than the mass in regular motion, and the Lyapunov reliability times of the major part of chaotic orbits are usually large when compared with the mean dynamical time of galaxies (Voglis, Stavropoulos & Kalapotharakos 2006). This means that the changes in the modelled structures caused by these orbits are small during Hubble time-scales, and the persistence of

the models seems to be assured. Typical computer precision values may be set as $\delta \sim 10^{-16}$, and following equation (3), the returned predictability times assure the goodness of the computations for very long times, in agreement with the above. Regardless of this result, it must be taken into account that because the exponential dependency of equation (3), there may be transients with lower predictability indexes, and values of $h \sim 0.1$ lead to extremely short predictability times.

Finite-time Lyapunov exponents techniques are indeed useful for studying those transient periods that the dynamics may suffer before ending in a final invariant state. The distributions can be built using shorter total integration times than those required for reaching the asymptotic behaviour. There is a limitation, however, when reducing the total integration time, that is the number of finite intervals needed for having good statistics values derived from the distribution. As Δt increases, the number of intervals needed for building a well sampled distribution and a reliable mean, deviation or kurtosis calculation also increases.

We have used integration times as long as 10^5 Gyr. To integrate over such long times is a matter of discussion. Using a Hubble constant $H_0 \sim 71$ km s^{-1} Mpc^{-1} we have a Hubble time $t_H \sim 13.8$ Gyr. One can argue about the physical meaning of using integration times some orders of magnitude larger than t_H. Simple simulations which consider static potentials should be constrained to times about 5 Gyr, as we do not know the evolution of the galaxies beyond than that (Martinez-Valpuesta & Shlosman 2004), and long integration lasting several times the age of the Universe should take into consideration that the galaxies may have evolved and disappeared at those time-scales. But one may argue that those long integrations can be read as the sum of individual integrations, each one sized Δt. Considering that the initial conditions are reset every Δt, the galaxy model can be considered valid. Indeed, we have seen in the Milky Way case that the intervals can be very small in the cases with lower predictabilities. For these small lengths, we can use even shorter total integrations times and still get similar results.

Regarding the selection of the finite-time intervals sizes, we have observed that, conversely to the dissipative case, the time-scales when the deviation vectors leave the local regime of the flow and begin to evolve under the global dynamics can be different and smaller than the time-scales where the asymptotic regime starts. When Δt is large enough, the distributions tend to shrink and

centre around the asymptotic value. In early works of Contopoulos, Grousousakou & Voglis (1995), the interval length (characteristic time) for the effective exponents was t_H. We have seen that it is possible to use intervals smaller than t_H for gaining insight into the properties of the flow.

The method presented in this paper indicates the most adequate interval length for estimating the predictability of a given orbit, independent of their regular or irregular nature. When there are several dynamical transients, reflected in changes in the shapes of the finite-time distributions, and consequently, different zero-crossings in the kurtosis curves, this method returns upper limits to the orbit predictability.

The dynamical times are different depending on the studied orbit and model. The predictability indexes values can be used for comparing the predictability of different orbits. They reflect how the shadowing time increases as the precision in the computations increases. Low predictability indexes lead to short shadowing times. Selecting an integration scheme and assuring the energy is kept constant in time (within some small error) does not imply the calculated orbit is shadowed by a real one beyond certain limits.

The predictability index estimates this shadowing time duration. A given numerical scheme with certain precision can be enough when the shadowing times are large. But this may be not the case when the shadowing times are shorter. A high predictability index may indicate that high-precision time-consuming schemes are not necessary, even for chaotic orbits. Indeed, Runge–Kutta order 4 (RK4) integrators provide good results even for the strongest chaotic orbits seen in the presented meridional potentials. Conversely, a low predictability index points to the use of more powerful schemes, as required in the Milky Way model. In a general case, when these indexes are really small, large increases in precision does not mean large increases in shadowing times, and one should consider the cost of implementing more complex and time-consuming schemes.

The percentages of regular and chaotic orbits in the phase space are not only a function of its spatial location but also a function of the total energy and main parameters of the model (Manos & Athanassoula 2011), and the amount of chaotic and regular motions in a given ensemble of initial conditions is related to the forecast of its predictability. Chaos detection methods based on saturation or averaging return different values as the saturation times vary because of the possible evolving presence of different regions of chaos, moderate or strong (Maffione et al. 2013). We have estimated the finite-time lengths to use in the calculation of the h-index, from the analysis of changes in the shapes of the distributions. When several zero crossings are present, we have selected the zero based on the Poincaré section crossing time-scales (see Table 2). This method has been applied to regular and chaotic orbits, and the results point to the validity of the shadowing times returned by equation (3) even when the ergodic diffusion model may not be fully applicable in the regular cases.

Our work has focused on the predictability index as estimator of the accuracy of an orbit in some time-independent potentials. The time independence of such potentials allows the trajectories to be either periodic, regular or chaotic (strong or weak). But the only unusual transitions found are those when a chaotic trajectory behaves like a regular orbit and requires long time-scales to reveal its true chaotic nature. In time-dependant potentials, one can find migrations from chaotic to regular (Manos & Machado 2014). Our method is applicable both when there are changes from regular to chaotic motions, or changes from chaotic to regular motions, as in the time-dependant cases. This is because the predictability index presented in this paper derives from solving the variational

equations and detecting changes in the shapes of the finite-time Lyapunov exponents as the finite-time intervals are increased. The calculation of the predictability indexes for a set of initial conditions on a given model, and the analysis of the results as its control parameters vary and these percentages evolve, is an interesting research topic to extend our results.

We have analysed the predictability of several orbits, weakly or strongly chaotic, with the notion *weak* or *strong* associated with have a relatively smaller or larger value of the asymptotic Lyapunov exponent λ. A final point to discuss is the possible applicability of these techniques for the analysis of irregular, yet not chaotic orbits. Notice that the term weak chaos is not universal, and these dynamical systems showing irregular dynamics where the separation of nearby trajectories grows weaker than exponential, implying zero Lyapunov exponents, are sometimes referred as weakly chaotic systems (Klages 2013).[2]

In these systems, there is no equivalence between time and ensemble averages. This weak ergodicity breaking means that a random sampling of the invariant distribution should not have the same content statistically as a single orbit integrated for extremely long times. We note here that studies analysing whether the Lyapunov exponents are zero or not can be useful for distinguishing between chaotic or not chaotic orbits, but not for distinguishing irregular non-chaotic orbits. An irregular motion is chaotic if it is bounded, the ω-limit set does not merely consist in connecting arcs and there is at least one asymptotic positive Lyapunov exponent (Alligood, Sauer & Yorke 1996). Conversely, a regular orbit has vanishing Lyapunov exponents. However, it is not clear whether an irregular orbit will necessarily have at least a non-zero real exponent. Although it is generally assumed that irregular orbits and chaotic orbits are the same in Hamiltonian systems, this has not been proven in general (Carpintero & Aguilar 1998). We note here our work relies on the characterization of the predictability of a given orbit, independent of its chaotic, regular or irregular nature.

ACKNOWLEDGEMENTS

REFERENCES

Alligood K., Sauer T. D., Yorke J. A., 1996, Chaos: An Introduction to Dynamical Systems. Springer-Verlag, New York

Athanassoula E., Romero-Gómez M., Bosma A., Masdemont J. J., 2010, MNRAS, 407, 1433

Binney J., Tremaine S., 1987, Galactic Dynamics. Princeton Univ. Press, Princeton, NJ

Cachucho F., Cincotta P. M., Ferraz-Mello S., 2010, Celest. Mech. Dyn. Astron., 108, 35

Caranicolas N. D., Zotos E. E., 2010, Astron. Nachr., 331, 330

Carpintero D. D., Aguilar L. A., 1998, MNRAS, 298, 21

Carpintero D., Muzzio J. C., Navone H. D., 2014, MNRAS, 438, 287

[2] There are more uses for the term weak chaos. Some papers use this term when there is a smaller Lyapunov exponent, or two sets of trend values (Mulansky et al. 2011). Others use it when the phase-space dynamics is mainly regular with just a few chaotic trajectories and the dynamics is strongly dependent, in a very complex way, on the chosen initial condition (Custodio, Manchein & Beims 2012).

Casertano S., Ratnatunga K. U., Bahcalli J. N., 1990, ApJ, 357, 435
Chiba M., Beers T. C., 2001, ApJ, 549, 325
Cincotta P. M., Giordano C. M., 2008, in Perlidze T. B., ed., New Nonlinear Phenomena Research. Nova Science Publishers, Inc., New York, p. 319
Cincotta P. M., Simó C., 2000, A&AS, 147, 205
Contopoulos G., 1970, AJ, 71, 96
Contopoulos G., Harsoula M., 2013, MNRAS, 436, 1201
Contopoulos G., Grousousakou E., Voglis N., 1995, A&A, 304, 374
Custodio M. S., Manchein C., Beims M. W., 2012, Chaos, 22, 026112
Froeschlé C., Lega E., 2000, Celest. Mech. Dyn. Astron., 78, 167
Grassberger P., Badii R., Politi A., 1988, J. Stat. Phys., 51, 135
Hairer E., Norsett S. P., Wanner G., 1993, Solving Ordinary Differential Equations I. Nonstiff Problems. Springer Series in Computational Mathematics, Vol 8. Springer-Verlag, Berlin
Hayes W. B., 2003, ApJ, 587, L59
Hénon H., Heiles C., 1964, AJ, 69, 73
Johnston K. V., Spergel D. N., Hernquist L., 1995, ApJ, 451, 598
Kantz H., Grebogi C., Prasad A., Lai Y. C., Sinde E., 2002, Phys. Rev. E, 65, 026209
Klages R., 2013, in Leoncini X., Leonetti M., eds, From Hamiltonian Chaos to Complex Systems. Springer-Verlag, Berlin, p. 3
Law D. R., Majewski S. R., Johnston K. V., 2009, ApJ, 703, L67
Lichtenberg A. J., Lieberman M. A., 1992, Regular and Chaotic Dynamics, 2nd edn. Applied Mathematical Sciences, Vol. 38. Springer-Verlag, New York
Maffione N. P., Darriba L. A., Cincotta P. M., Giordano C. M., 2013, MNRAS, 429, 2700
Manos T., Athanassoula E., 2011, MNRAS, 415, 629
Manos T., Machado R. E. G., 2014, MNRAS, 438, 2217
Martinez-Valpuesta I., Shlosman I., 2004, ApJ, 613, L29
Miyamoto M., Nagai R., 1975, PASJ, 27, 533
Mulansky M., Ahnert K., Pikovsky A., Shepelyansky D. L., 2011, J. Stat. Phys., 145, 1256

Newman W. I., Lee A. Y., 2005, BAAS, 37, 531
Olle M., Pfenigger D., 1998, A&A, 334, 829
Ott W., Yorke J. A., 2008, Phys. Rev. E, 78, 056203
Papaphilippou Y., Laskar J., 1998, A&A, 329, 451
Pfenigger D., 1984, A&A, 134, 373
Pichardo B., Martos M., Moreno E., 2004, ApJ, 609, 144
Sandor Z., Erdi B., Szell A., Funk B., 2004, Celest. Mech. Dyn. Astron., 90, 127
Sauer T., 2002, Phys. Rev. E, 65, 036220
Sauer T., Grebogi C., Yorke J. A., 1997, Phys. Rev. Lett. A, 79, 59
Schwarzschild M., 1993, ApJ, 409, 563
Skokos Ch., 2001, J. Phys. A, 34, 10029
Skokos Ch., Patsis P. A., Athanassoula E., 2002, MNRAS, 333, 847
Skokos Ch., Bountis T. C., Antonopoulos Ch., 2007, Physica D, 231, 30
Stuchi T. J., 2002, Brazilian J. Phys., 32, 958
Szezech J. D., Jr, Schelin A. B., Caldas I. L., Lopes S. R., Morrison P. J., Viana R. L., 2013, Phys. Lett. A, 377, 452
Tsiganis K., Varvoglis H., Hadjidemetriou J. D., 2002, Icarus, 155, 454
Vallejo J. C., Sanjuan M. A. F., 2013, New J. Phys., 15, 113064
Vallejo J. C., Aguirre J., Sanjuan M. A. F., 2003, Phys. Lett. A, 311, 26
Vallejo J. C., Viana R., Sanjuan M. A. F., 2008, Phys. Rev. E, 78, 066204
Viana R. L., Grebogi C., 2000, Phys. Rev. E, 62, 462
Voglis N., Contopoulos G., Efthymiopoulos C., 1999, Celest. Mech. Dyn. Astron., 73, 211
Voglis N., Stavropoulos I., Kalapotharakos C., 2006, MNRAS, 372, 901
Wang Y., Zhao H., Mao S., Rich R. M., 2012, MNRAS, 427, 1429
Ziehmann C., Smith L. A., Kurths J., 2000, Phys. Lett. A, 271, 237
Zotos E. E., 2014, A&A, 563, 19
Zotos E. E., Caranicolas N. D., 2013, A&A, 560, 110

This paper has been typeset from a TeX/LaTeX file prepared by the author.